Rotorcraft Aeroelastic Analysis using Dynamic Wake/Dynamic Stall Models and its Validation

(Received: Feb. 1, 2014. Revised: May 31, 2014. Accepted: Aug. 25, 2014)

M. Rohin Kumar [1]
C. Venkatesan[2]

Abstract
Accurate prediction of helicopter loads and response requires the development of a multi-disciplinary comprehensive analysis program. Helicopter loads and response is an aeroelastic problem as it involves interaction of the structural, inertia and aerodynamic operators. The objective of this paper is to describe the development of a comprehensive analysis code for helicopter aeroelastic analysis and present some of the validation studies. The helicopter modeled is a conventional one with a hingeless single main rotor and single tail rotor. The blade undergoes flap, lag, torsion and axial deformations and is modeled using beam finite elements. Tip sweep, pretwist, precone, predroop, torque offset and root offset are included in the model. Aerodynamic model includes Peters-He dynamic wake theory for inflow and the modified ONERA dynamic stall theory for airloads calculations. The complete 6-dof nonlinear equilibrium equations are solved for analyzing general flight conditions including steady maneuver. Validation studies presented in this paper include comparison of experimental data with the analysis results pertaining to (i) structural dynamics of swept-tip beams, (ii) whirl tower test, and (iii) steady forward flight trim state of a helicopter. Results of a study showing the effects of the blade geometric parameters on the performance, response and loads of the rotor are also given.

1 Introduction

Helicopter analysis is a multi-disciplinary field involving rotary-wing aeroelasticity as well as flight dynamics. The complexity of the problem requires the development of a comprehensive analysis program that integrates all the disciplines involved in the study [1]. A truly comprehensive helicopter analysis program should be capable of calculating performance, loads, vibrations and handling qualities of the aircraft.

Rotary-wing aeroelasticity involves the study of interaction between the structural, inertia and aerodynamic operators. For accurate analysis, all the operators need to be modeled accurately. The structural dynamic modeling of the coupled bending, torsion, and axial deformation of helicopter rotor blades has already reached a high level of maturity making use of finite element or multibody techniques. With rotor blades incorporating tip sweep and anhedral angles for performance improvement, later structural dynamics models have accounted for these advanced geometry effects [2, 3]. The aerodynamic operator formulation involves the determination of the inflow at various locations of the rotor blade and then the calculation of the airloads. Methods for calculating the inflow range in complexity from the uniform inflow model to dynamic inflow/wake [4] and free-wake models. A complicated aspect of the unsteady aerodynamics environment of the rotor blade section is the dynamic stall phenomenon. For accurate results, dynamic stall modeling has to be included in the formulation for airloads calculation. It is difficult to predict stall and its effects using theoretical unsteady aerodynamic tools. Hence, many researchers still depend on empirical or semi-empirical models. Two primary semi-empirical dynamic stall models exist today the ONERA model [5] and the Leishman-Beddoes model. A comprehensive review of the state of art in rotorcraft CFD/CSD coupling for

[1] Senior Research Engineer, Dept. of Aerospace Eng., Indian Institute of Technology, Kanpur, India
[2] Professor, Dept. of Aerospace Eng., Indian Institute of Technology, Kanpur, India

doi:10.3293/asdj.2013.25

trimmed aeroelastic loads solution in forward flight is given in [6]. While development of this field can have major benefits in the prediction of rotor loading in the long run, the need for simpler, less-time consuming models for real-time simulations persists. In [7], a new reduced-order dynamic stall modeling approach that retained the fidelity of CFD while maintaining the computational efficiency of the semi-empirical models has been presented as a potential enabling methodology for comprehensive rotorcraft analysis.

Several comprehensive analyses are used both in academia and in the industry today. These analyses include analytical tools such as finite element analysis, multi-body systems analysis, dynamic inflow analysis, free-wake analysis and techniques for coupling CFD with rotorcraft comprehensive analyses for loads calculation. Some of the better known comprehensive analyses today are the 2GCHAS and the RCAS developed by the US Army, CAMRAD developed by Johnson, UMARC developed at the University of Maryland, FLIGHTLAB developed by Advanced Rotorcraft Technology, Inc., RDyne developed at Sikorsky Aircraft and the multibody systems technology based DYMORE and MBDyn developed in academia. While there are other equally well-known analyses available, the engineering background of these codes are not easily available in the open literature. An extensive history of comprehensive analyses has been given in [8].

In [9], a computational aeroelastic model was formulated for the prediction of trim and response of a helicopter rotor system. However, the study was limited to steady, level flight. The objective of this paper is to describe the development of a comprehensive aeroelastic model for a conventional helicopter incorporating a most general structural model for the rotor blade including fuselage rigid body dynamics, aerodynamic model with Peters-He for inflow and modified ONERA for airloads. The focus, here, is on integration of various existing component theories, solution methodology and systematic validation of the formulation. This aeroelastic model formed the basis for studying and breaking new ground in maneuvering flight, control response and blade-tip geometry effects [10–12]; however, these topics are beyond the scope of this paper. While many of the individual topics mentioned have been covered in detail by other researchers, a unified coverage of all these elements has been very few. The sections to follow detail the different components of the model, the solution procedure and some results compared with experimental data for validation.

2 Blade Structural Model

An elastic rotating beam with constant angular velocity was considered. Blade sweep, precone, predroop, pretwist, root offset and torque offset are included in the model. The beam consists of a straight portion and a tip with sweep and anhedral(droop) angles relative to the straight portion as shown in Fig. 1. By convention, backward sweep and dihedral angles have been taken as positive. The cross-section of the blade has a general shape with distinct shear center and center of mass. Several coordinate systems, shown in Figs. 2, and their transformation matrices were defined to fully describe the geometry and deformation of the rotating blade. The non-linear kinematics of deformation was based on the mechanics of curved rods (small strains and finite rotations) with appropriate provision for cross-sectional shear and out-of-plane warping [13]. For the most part, the blade structural formulation in this paper follows the approach in [3].

2.1 Equations of Motion

The nonlinear equations of motion and the corresponding finite element matrices are derived for each beam element using Hamilton's principle:

$$\int_{t_1}^{t_2} (\delta U - \delta T - \delta W_e) dt = 0 \tag{1}$$

where U, T, W_e represent the strain energy, kinetic energy, and virtual work of external loads, respectively and ∂ represents a variation. The variation of the strain energy for each beam element can be calculated as

$$\delta U_i = \frac{1}{2} E_0 R^3 \int_0^{(l_e)_i} \int\int \left\{ \begin{array}{c} \delta\epsilon_{xx} \\ \delta\gamma_{x\eta} \\ \delta\gamma_{x\zeta} \end{array} \right\}^T \left\{ \begin{array}{c} \sigma_{xx} \\ \sigma_{x\eta} \\ \sigma_{x\zeta} \end{array} \right\} d\eta \; d\zeta \; dx \tag{2}$$

The simplified strain-displacement relations are given as follows:

$$\begin{aligned}
\epsilon_{xx} &= u_{k,x} + \frac{1}{2} v_{k,x}^2 + \frac{1}{2} w_{k,x}^2 + \frac{1}{2}(\eta^2 + \zeta^2)\phi_{k,x}^2 \\
&\quad - \Psi \phi_{k,xx} - \tau_0 (\zeta \Psi_{,\eta} - \eta \Psi_{,\zeta}) \phi_{k,x} \\
&\quad - [\eta \cos(\theta_G + \phi) - \zeta \sin(\theta_G + \phi)] v_{k,xx} \\
&\quad - [\eta \sin(\theta_G + \phi) + \zeta \cos(\theta_G + \phi)] w_{k,xx} \\
\gamma_{x\eta} &= -(\psi_\eta + \zeta)\phi_{k,x} - \zeta \phi_0 \\
\gamma_{x\zeta} &= -(\psi_\zeta - \eta)\phi_{k,x} + \eta \phi_0
\end{aligned} \tag{3}$$

Where,

$$\phi_0 = (v_{k,xx} \cos\theta_G + w_{k,xx} \sin\theta_G)(-v_{k,x} \sin\theta_G + w_{k,x} \cos\theta_G)$$

The variation of kinetic energy for each beam element is calculated as

$$T = \frac{1}{2} \int_V \rho \vec{V}.\vec{V} dV \tag{4}$$

where the velocity vector for any beam element includes contribution from the rigid-body motion of the fuselage. Integrating the above volume integrals for strain and kinetic energies over the cross-section results in line integrals. The cross-sectional integrals provide the sectional properties of the rotor blade.

2.2 Finite Element Discretization

The partial differential equations of motion obtained using Hamiltons principle are dependent on both space and time. The spatial discretization of the equations is done using the finite element method. The blade is modeled by a series of straight beam finite elements along the elastic axis of the blade. Two finite elements at the tip were used to model the sweep and anhedral. Each finite element in the tip can be given a sweep angle and/or anhedral angle independent of the other. Each beam element consists of two end nodes and one internal node at its mid-point, resulting in 14 degrees of freedom representing 4 lag, 4 flap, 3 torsional and 3 axial motion variables. This is shown in Fig. 3. Cubic Hermite interpolation polynomials are used for the bending displacement, while quadratic Lagrangian interpolation polynomials are used for torsional rotation and axial deflections. Applying Hamiltons principle to each finite element results in a discretised form of the equations of motion. Special care has been taken in the treatment of the axial degree of freedom and in the integration of the swept tip mass and stiffness element matrices into the global matrices [14]. Panda [14] derived general transformation and constraint relations between two blade elements joined at an angle to each other. The importance of including nonlinearities in transformations was pointed out, especially for large sweep angles. In the current model, the constraint relation is that the tip sweep or anhedral angle does not change after deformation.

The beam element matrices associated with kinetic energy variation are obtained by substituting the derived kinematic velocity expression and the assumed expressions for the displacement functions in the kinetic energy variation, δT_i (Eq. 4) and carrying out the integration over the length of the beam element. The resulting variation of the kinetic energy can be written in the form:

$$\begin{aligned}
\delta T_i \quad = \quad & -\{\delta \mathbf{q}\}^T([M]_{14\times 14}\{\ddot{\mathbf{q}}\} + [M^C]_{14\times 14}\{\dot{\mathbf{q}}\} + [K^{cf}]_{14\times 14}\{\mathbf{q}\} \\
& +[M^1]_{14\times 3}\left\{\begin{array}{c} \dot{u_f} \\ \dot{v_f} \\ \dot{w_f} \end{array}\right\} + [M^2]_{14\times 3}\left\{\begin{array}{c} u_f \\ v_f \\ w_f \end{array}\right\} + [M^3]_{14\times 3}\left\{\begin{array}{c} \dot{p_f} \\ \dot{q_f} \\ \dot{r_f} \end{array}\right\} \\
& +[M^4]_{14\times 3}\left\{\begin{array}{c} p_f \\ q_f \\ r_f \end{array}\right\} + \{V^L\}_{14\times 1} + \{V^{NL}\}_{14\times 1}) \qquad (5)
\end{aligned}$$

where q represents the vector of unknown nodal degrees of freedom

$$\{\mathbf{q}\}_{14\times 1} = \left\{ \begin{array}{cccccccccccccc} v_1 & v_1' & v_2 & v_2' & w_1 & w_1' & w_2 & w_2' & u_1 & u_2 & u_3 & \phi_1 & \phi_2 & \phi_3 \end{array} \right\}^T$$

and [M] is the mass matrix, $[M^C]$ is a Coriolis damping matrix, $[K^{cf}]$ is a centrifugal stiffness matrix. $[M^1]$, $[M^2]$, $[M^3]$ and $[M^4]$ are contributions due to the fuselage and hence called the fuselage matrices. $[V^L]$ and $[V^{NL}]$ are vectors arising from linear and non-linear terms, respectively, in the kinetic energy variation. The elemental matrices associated with the strain energy variation are derived by substituting the assumed expressions for the displacement function in the strain energy variation δU_i (Eq. 2) and carrying out the integration over the length of the element. The resulting variation of the strain energy can be written in the form:

$$\delta U_i = \{\delta \mathbf{q}\}^T([K^E]\{\mathbf{q}\} + \{F^E\}) \qquad (6)$$

where, $\left[K^E\right]_{14\times 14}$ is the elemental stiffness matrix, $\left\{F^E\right\}_{14\times 1}$ is the nonlinear stiffness vector. By linearization of nonlinear terms associated with the axial strain at the elastic axis, the above nonlinear stiffness vector can be written in the following form as:

$$\{F^E\} = ([K^{E'}]\{\mathbf{q}\} + \{\tilde{F}^E\})$$

2.3 MAPLE™ Implementation

Traditional moderate deflection beam theories are based on ordering schemes. Coordinate transformations in the derivation of kinetic and strain energy contributions result in large number of terms. The ordering scheme allows one to neglect higher order terms in the structural, aerodynamic and inertia operators in order to bring down the number of terms to manageable quantity. However, ordering scheme is not unique or consistent and so, has to be applied with care and flexibility. In this work, the derivation of the beam equations of motion has been implemented in the symbolic computational tool MAPLE™. Usage of a symbolic package like MAPLE™ helps retain all the terms and reduce the approximations, thus eliminating the need for ordering schemes.

The extensive algebraic manipulation involved in the derivation of the exact kinematics of the elastic motion, and in the derivation of the kinetic energy and strain energy expressions needed for forming the element matrices were taken care of in MAPLE™. Using this tool, trigonometric identities and term cancellations can be applied to manipulate the algebra to seek as many simplifications as possible. A symbolic computational tool eliminates the need to simplify problems by hand. The expressions derived for forming the element matrices were then transferred to aeroelastic code which was implemented using C++.

3 Aerodynamic Model

The aerodynamic model involves the evaluation of inflow at various locations on the rotor disc and the evaluation of sectional aerodynamic loads on the rotor blade. While the comprehensive analysis program has been implemented as modular with multiple options for inflow and loads calculations, for the purpose of this paper, only the Peters-He model for inflow and the modified ONERA dynamic stall model for loads are discussed. Both these models, by virtue of their being formulated as a set of differential equations are very suitable for aeroelastic calculations.

The Peters-He dynamic inflow model is a compact formulation with multiple states that allow variation of the inflow in the radial as well as azimuthal directions. In this model, the total inflow is a function of azimuth, time, and radial station and is given as:

$$\lambda(\bar{r},\psi,t)=\sum_{p=0}^{\infty}\sum_{j=p+1,p+3,\cdots}^{\infty}\phi_j^p(\bar{r})\left[\alpha_j^p(t)\cos(p\psi)+\beta_j^p(t)\sin(p\psi)\right] \tag{7}$$

where $\alpha_j^p(t)$ and $\beta_j^p(t)$ are evaluated by solving a set of differential equations.

$$[M]\begin{Bmatrix}\vdots\\ \{\alpha_j^p\}\\ \vdots\end{Bmatrix}^{\cdot}+[V_c][\tilde{L}^c]^{-1}\begin{Bmatrix}\vdots\\ \{\alpha_j^p\}\\ \vdots\end{Bmatrix}=\frac{1}{2}\begin{Bmatrix}\vdots\\ \{\tau_n^{mc}\}\\ \vdots\end{Bmatrix} \tag{8}$$

and

$$[M]\begin{Bmatrix}\vdots\\ \{\beta_j^p\}\\ \vdots\end{Bmatrix}^{\cdot}+[V_s][\tilde{L}^s]^{-1}\begin{Bmatrix}\vdots\\ \{\beta_j^p\}\\ \vdots\end{Bmatrix}=\frac{1}{2}\begin{Bmatrix}\vdots\\ \{\tau_n^{ms}\}\\ \vdots\end{Bmatrix} \tag{9}$$

More details of these equations can be found in [4]. While the model allows for multiple states, for the analysis in this paper, three states (α_1^0, α_2^1 and β_2^1) were used. The ONERA model describes the unsteady airfoil behaviour in both attached flow and separated flow using a set of nonlinear differential equations. In the unstalled region, it is identical to Theodorsens unsteady aerodynamic theory except that the lift deficiency function C(k) is approximated by a first order rational approximation. The study in [15] concluded that replacing the first order rational approximation by a second order approximation results in a more accurate modified ONERA dynamic stall model, which shall be used in the present analysis. The modified dynamic stall model provides the time variation of lift, moment and drag on an oscillating airfoil. The stall model assumes that the lift, moment and drag are acting at the quarter chord point. The unsteady lift acting normal to the resultant velocity is given as:

$$L=\frac{1}{2}\rho\tilde{S}[sb\dot{W}_0+\tilde{k}b\dot{W}_1+V\Gamma_1+V\Gamma_2] \tag{10}$$

Where Γ_1, Γ_2 are evaluated using the following equations

$$\begin{aligned}
\ddot{\Gamma}_1+B_2(\frac{V}{b})\dot{\Gamma}_1+B_3(\frac{V}{b})^2\Gamma_1 &= A_3(\frac{V}{b})^2\frac{\partial C_{z_L}}{\partial\theta}W_0+A_3\sigma(\frac{V}{b})^2W_1\\
&\quad +A_2(\frac{V}{b})\frac{\partial C_{z_L}}{\partial\theta}\dot{W}_0+A_2(\frac{V}{b})\sigma\dot{W}_1\\
&\quad +A_1\frac{\partial C_{z_L}}{\partial\theta}\ddot{W}_0+A_1\sigma\ddot{W}_1\\
\ddot{\Gamma}_2+a_l(\frac{V}{b})\dot{\Gamma}_2+r_l(\frac{V}{b})^2\Gamma_2 &= -[r_l(\frac{V}{b})^2V\Delta C_z|_{W_0/V}+E_l(\frac{V}{b})\dot{W}_0]
\end{aligned}$$

The unsteady moment on the airfoil is given as:

$$M = \frac{1}{2}\rho\tilde{S}2b[V^2 Cm_L|_{W_0/V} + (\overline{\sigma}_m + d_m)b\dot{W}_0 + \sigma_m VW_1 + s_m b\dot{W}_1 + V\Gamma_{m2}] \quad (11)$$

Where Γ_{m2} is evaluated using the following equation

$$\ddot{\Gamma}_{m2} + a_m(\frac{V}{b})\dot{\Gamma}_{m2} + r_m(\frac{V}{b})^2\Gamma_{m2} = -[r_m(\frac{V}{b})^2 V\Delta Cm|_{W_0/V} + E_m(\frac{V}{b})\dot{W}_0]$$

The unsteady drag acting along the resultant velocity is given as:

$$D = \frac{1}{2}\rho\tilde{S}[V^2 Cd_L|_{W_0/V} + \sigma_d b\dot{W}_0 + V\Gamma_{d2}] \quad (12)$$

Where Γ_{d2} is evaluated using the following equation

$$\ddot{\Gamma}_{d2} + a_d(\frac{V}{b})\dot{\Gamma}_{d2} + r_d(\frac{V}{b})^2\Gamma_{d2} = -[r_d(\frac{V}{b})^2 V\Delta Cd|_{W_0/V} + E_d(\frac{V}{b})\dot{W}_0]$$

where ΔC_z, ΔC_m, and ΔC_d are the difference between the linear static aerodynamic coefficient extrapolated to the stalled region to actual static aerodynamic coefficient of lift, moment and drag respectively, measured at an effective angle of attack, W_0/V. The quantities $C_{m_L}|_{W_0/V}$, and $C_{d_L}|_{W_0/V}$ are the static moment and drag coefficients in linear regime measured at an effective angle of attack, W_0/V. The various constants defined in Eqs. 10-12 are given in [5].

4 Complete Aeroelastic Equation for the Rotor Blade

Comprehensive analysis of the rotary-wing aeroelastic behavior brings together the structural and aerodynamic models described in the previous sections. In addition to these models, in order to calculate the rotor aeroelastic response, a trim calculation procedure [16] needs to be added. The global aeroelastic equation for the whole blade is obtained by assembling the elemental matrices from the kinetic and strain energy contributions,

$$\begin{aligned}[M]\{\ddot{\mathbf{q}}\} + [C]\{\dot{\mathbf{q}}\} + [K]\{\mathbf{q}\} = \{F_{AD}\} + [M^1]\begin{Bmatrix}\dot{u}_g\\ \dot{v}_g\\ \dot{w}_g\end{Bmatrix} + [M^2]\begin{Bmatrix}u_g\\ v_g\\ w_g\end{Bmatrix}\\ +[M^3]\begin{Bmatrix}\dot{p}\\ \dot{q}\\ \dot{r}\end{Bmatrix} + [M^4]\begin{Bmatrix}p\\ q\\ r\end{Bmatrix} + \{V^L\} + \{V^{NL}\} \quad (13)\end{aligned}$$

where $\{F_{AD}\}$ is the aerodynamic force contribution. The above aeroelastic equation is transformed to the modal domain inorder to reduce the problem complexity. Solution of the nonlinear aeroelastic equation of the main rotor involves successively calculating the inflow, rotor loads and the resulting response for a small time step. The time is then incremented and the calculation process is repeated. This iteration on time continues until the converged periodic solution for steady-state flight is obtained. Combining all the forces and moments due to main rotor, tail rotor, fuselage and empennage, the fuselage dynamic equations of motion are obtained (three translational and three rotational equations of motion). The trim equations comprise the complete nonlinear vehicle force and moment equilibrium equations. Comprehensive analysis of the helicopter is, thus, a coupled rotor-fuselage analysis. Trim analysis involves iteration on the pilot controls and vehicle attitudes to achieve equilibrium of the net forces and moments at the centre of gravity of the helicopter.

5 Solution Procedure

Figure 4 shows the flow chart of the procedure used for the coupled rotor/fuselage trim analysis of a helicopter in general maneuvering flight. For maneuvering flight, trim analysis requires that certain quantities be prescribed in advance flight speed, flight path angle, spin rate and side slip angle. A propulsive trim procedure was adopted to obtain the main rotor control angles, tail rotor control angle and fuselage attitudes. The algorithm shown was implemented as a C++ program using the open-source GSL [17] as the math library. The differential equations were solved using the Runge-Kutta integration scheme while the non-linear algebraic trim equations are solved using the Newton-Raphson method. The algorithm consists of two iterative loops an inner-loop and an outer-loop. The inner-loop comprises three sets of differential equations representing blade sectional loads, rotor inflow and blade response. The airloads and inflow are evaluated at alternate time-steps (loads are evaluated at 0^0, 9^0, 18^0 azimuth locations and inflow is evaluated at 4.5^0, 13.5^0, 22.5^0.azimuth locations). The outer-loop solves the trim problem which is a set of nonlinear algebraic equations. Thus the inner-loop concerns the rotor blade aeroelastic response while the outer-loop considers the vehicle as a whole. The program outputs the inflow over the rotor, hubloads, blade response, blade sectional loads, blade shear and bending moments, rotor pilot inputs and the vehicle attitudes.

6 Validation Studies

6.1 Structural Dynamics Validation

Results, obtained using the current model, have been validated against experimental as well as analytical data which are described below.

6.1.1 Maryland Vacuum Chamber Experiment

This is a set of experimental data obtained by the Department of Aerospace Engineering at the University of Maryland. The University of Maryland data [18] provides the rotating frequencies of a blade with the outboard 16% swept at various angles. Although the experiment included both composite and a uniform aluminum beams, for the purpose of this paper, only the uniform aluminum beam results are used. Figure 5 gives the geometrical details of the clamped beam used in the experiment. It may be noted that the width of the tip decreases with respect to the straight portion by a factor of the cosine of the sweep angle. In [19], in order to validate the then newly developed RCAS program, the analytical results obtained were compared with the Maryland experiment results. These analytical results have been included in this paper for comparison with the current model.

6.1.2 Effect of Sweep and Rotational Speed

The influence of sweep and rotational speed on the natural frequencies of the uniform aluminum beams with tip sweep are shown in Figs. 6-7. While the current model calculates all the flap, lag, torsional and axial frequencies and modes, only the relevant modal frequencies are compared with the data in [18]. The experimental data in this reference was given for natural frequencies in five flap-modes and one torsion mode as a function of sweep and rotational speed. The beams had sweep angles of $0^0, 15^0, 30^0$ and 45^0 and were rotated at 0, 500 and 750 RPMs. In Figs. 6-7, the results from the current model are shown as continuous lines with symbols. The experimental data and results from [19] are shown as star and square symbols respectively.

Figure 6 shows the effect of rotational speed on straight blade natural frequencies. It can be seen that frequencies obtained with the current model compare well with both experimental and RCAS values. For correlation purposes, the 3^{rd} mode of the current analysis, which is observed to be a lag mode, also has been included in the figure. A point to note is that the frequency at 750 RPM, which is labeled as 2^{nd} Flap in [18], coincides with the 3^{rd} mode of the current analysis. Figure 6 shows the rotational speed effect on a blade with a 45^0 tip sweep. There is good correlation between the current model and the experiment data for all cases except that the 3rd flap is over-predicted by about 15% at 750 RPM. Figure 7 shows the effect of tip sweep on non-rotating blades. In the torsion mode, the current model correlates well with the experimental values, except for the 300 tip sweep. Even in the case of 750 RPM, shown in Fig. 7, the torsion mode frequency for 300 tip sweep from the current model is offset from the experiment value by about 9%. From these two figures, it is seen that the effect of sweep is seen mostly in the higher frequencies and especially, in the torsion mode.

6.2 Validation with Whirl Tower Test Data

One of the ways to evaluate the aerodynamic characteristics of a rotor, experimentally, is the whirl tower test. To simulate a whirl tower, the main rotor trim inner loop section of the flowchart in Fig. 4 was carried out till convergence for different collective angles of a stand-alone rotor. The geometry of the rotor for which whirl tower test was carried out is given in Table 1 in appendix. From Fig. 8, it can be seen that the thrust and power values from the analysis match with the test data fairly well. Figure 9 shows the variation of root bending moment in flap and lag directions with respect to collective pitch angle of the rotor blade. The blade, being at a predroop angle from the hub-plane, undergoes positive flap bending moment at lower collective angles and at higher collective angles, flap bending moment turns negative, as seen in Fig. 9. The cross-over point (positive to negative) for flap bending moment is predicted to be 7.1 degrees collective while the test data is 7.7 degrees. In the lead-lag direction, the torque offset of the blade causes it to experience high inertia forces in the positive y-direction and this gives it a positive lead-lag moment at lower collective angles. At higher collective angles, as the aerodynamic drag increases, the lead-lag moment turns negative. For lead-lag bending moment, the cross-over point is predicted to be 5.0 degrees while the test data is around 3.7 degrees, as shown in Fig. 9.

6.3 Effects of Blade Configuration Parameters

As has been mentioned, the structural model has various options built-in in the form of geometric parameters like tip sweep, torque offset, precone, predroop etc. The general effects of most of these parameters are well-known today. For example, precone and predroop are used by the rotor designer as a means to reduce steady flap bending stresses for a hingeless rotor. Similarly, torque offset is employed to balance the torque of the rotor with the blade centrifugal force. The effects of precone and droop on the steady state blade loads of a small-scale two-bladed, untwisted rotor was experimentally studied in [20]. It was found that the lead-lag bending moments with negative droop (upward inclination) are reduced compared to those with precone. It was suggested that this was because of the introduction of the lead-lag displacement due to blade pitch change in the case of blade droop while this was absent in the case of precone. Positive blade-pitch angles produce a corresponding lag displacement and centrifugal force acts to lead the blade back to a radial direction imparting a positive increment in lead-lag bending moment. In [21], for the TIGER main rotor system, a hub geometry change from a 2.5 degrees blade droop angle to a central 2.5 degrees hub precone angle was performed to expand the load factor capability by lowering loads in lead-lag bending and in the control system. A systematic investigation of the effects of tip sweep and tip anhedral on the helicopter rotor blade response and loads was conducted in [2]. It was concluded that tip sweep reduces flap and torsional oscillatory responses while tip anhedral has considerable influence on flap dynamics. In this paper, for conciseness, only precone, predroop, presweep and torque offset are considered. The effects of varying each of these parameters on rotor response and loads is studied in the isolated rotor configuration for different collective pitch setting. Here, only those results which demonstrate the effects of these parameters on blade response and loads are presented. Figures 10 show the effects of precone (2.5 deg), predroop (2.5 deg) and presweep (2.5 deg) on the response of the blade. For the isolated rotor with only collective angle variation, it is seen that precone and predroop results are almost identical. As expected, these parameters reduce the flap response at higher positive collective (pitch) angles. However, this comes at the cost of a slight increment in the lag displacement. Presweep causes a slight reduction in the lag displacement and a slight increment in the flap displacement. Figures 11 show the effects of the above parameters on blade root lag and flap bending moments. They follow a similar trend as the blade response. Precone and predroop cause a reduction of the flap root bending moment at higher collective angles but increase the lag root bending moment. Presweep causes a slight reduction in the root lag bending moment and a slight increment in the root flap bending moment. Figures 12 show the effect of torque offset on the lag displacement and the root lag bending moment. As can be seen, introducing a small torque offset of 0.01m at the hub drastically reduces the lag displacement and the lag root bending moment.

6.4 Trim validation with flight test data

Figure 13 shows the variation of trim angles with speed in level forward flight. The vehicle and blade properties are given in Table 1 in the appendix. The analytical results have been correlated with the experimental data from [22]. The main rotor collective, tail rotor collective and the main rotor lateral cyclic angles are in good agreement with the flight test data. The hump in the lateral cyclic angle variation with forward speed is, especially, well predicted. However, the main rotor longitudinal cyclic and the vehicle pitch and roll attitudes have been overpredicted. A possible cause for the discrepancy in the longitudinal cyclic and vehicle pitch attitude correlation could be the main rotor wake interference with the empennage surfaces, which was not modeled. All the predicted trim variables deviate from the flight test data at higher speeds.

7 Concluding Remarks

In this paper, a comprehensive aeroelastic formulation was presented for a six degree-of-freedom helicopter with a conventional single main rotor and single tail rotor. This was achieved by incorporating a coupled flap-lag-torsion-axial rotor motion model, the Peters-He inflow model, a modified ONERA dynamic stall model along with a rigid fuselage model. The structural and aerodynamic models as well as the solution procedure of the aeroelastic formulation were validated by comparing the analysis results with experimental data pertaining to: (i) structural dynamics of swept-tip beams, (ii) whirl tower test, and (iii) steady forward flight trim state of a helicopter. The results of the structural dynamic analysis show good correlation with the experimental data as well as with analytical results of another comprehensive analysis program, RCAS. The performance characteristics of the rotor were well predicted by the current analysis as the comparison with whirl tower test data show. The root bending moments predicted by the analysis for the whirl tower rotor show reasonable correlation with the available test data. The influence of the blade geometric parameters on performance, response and loads of the rotor under hover conditions was also studied. The analytical results were mostly in-line with the known trends which further supports the validity of the formulation. In forward flight results, most of the trim variables are observed to be in good agreement with the flight test data. The hump in the lateral cyclic angle variation with forward speed is, especially, well predicted. However, a few deficiencies exist and these may be addressed in future work.

Nomenclature

a	torque offset or lift curve slope
a_d, a_l, a_m	parameters used in dynamic stall model
c	blade chord $(= 2\ b)$
$C(k)$	Theodorsen's lift deficiency function
C_d	drag coefficient
C_{d_L}	linear static drag coefficient extrapolated to the stall region
C_{m_L}	linear static moment coefficient extrapolated to the stall region
C_w	weight coefficient
C_{z_L}	linear static lift coefficient extrapolated to the stall region
$C_{l\alpha}, C_{l\alpha t}$	lift-curve slope for main and tail rotors
$\Delta C_z, \Delta C_m, \Delta C_d$	difference between extrapolated linear static coefficients and measured static coefficients
D	drag on airfoil or fuselage drag
e_1, e_2	root offset
E	modulus of elasticity
E_d, E_l, E_m	parameters used in dynamic stall model
$\{F_{AD}\}$	aerodynamic force vector
G	shear modulus
$[K^{cf}]$	centrifugal stiffness matrix
$[K^E]$	linear stiffness matrix
$[K^{E'}]$	nonlinear stiffness matrix
L	lift on airfoil
L_C	circulatory lift
L_{NC}	noncirculatory lift
$[L]$	coupling or gain matrix
L, M, N	steady moments acting at center of gravity of helicopter
M	moment on airfoil about elastic axis or Mach number
$[M]$	mass matrix or apparent mass matrix in inflow model
$[M^C]$	Coriolis damping matrix
$[M^1], [M^2]$	matrices related to vehicle translational motion defined in the expression of kinetic energy variation
$[M^3], [M^4]$	matrices related to vehicle angular motion defined in the expression of kinetic energy variation
M_∞	Mach number
N_b	number of blades in main rotor
N_{bt}	number of blades in tail rotor
O_H	hub center
p_f, q_f r_f	angular velocity components at c.g of helicopter
r_d, r_l, r_m	parameters used in dynamic stall model
R	main rotor blade radius
s, s_m	parameters used in dynamic stall model
T	main rotor thrust force or kinetic energy
u_f, v_f w_f	translational velocity components at c.g of helicopter
u_k	axial deformation of k^{th} blade
U	strain energy
u_1, v_1, w_1, ϕ_1, u_2, v_2, w_2, ϕ_2, v_1', w_1', v_2', w_2', u_{12}, ϕ_{12}	element nodal degrees of freedom

$\{U\}$,$\{V\}$,$\{W\}$,$\{\Phi\}$	vectors of element nodal degrees of freedom
v_k	lead-lag deformation of k^{th} blade
V	oncoming velocity
V_{CG}	velocity at c.g of helicopter
$\{V^L\}$	inertia and linear vector defined in the expression of kinetic energy variation
$\{V^{NL}\}$	nonlinear vector defined in the expression of kinetic energy variation
$[V]$, $[V_c]$, $[V_s]$	velocity matrices used in dynamic inflow models
w_k	flap deformation of k^{th} blade
W	weight of the helicopter
W_e	external work due to nonconservative forces
x_k	coordinate along k^{th} blade axis
α	warping amplitude
α_j^p, β_j^p	induced flow coefficients
β_d	blade predroop angle
β_p	blade precone angle
β_s	blade presweep angle, helicopter sideslip angle
χ	wake skew angle
ϵ_{xx}	normal strain component
ϕ_k	elastic twist of k^{th} blade
Φ	fuselage attitude in roll
γ	lock number
$\gamma_{x\eta}$,$\gamma_{x\zeta}$	transverse shear strain components
$\overline{\gamma}_{x\eta}$,$\overline{\gamma}_{x\zeta}$	transverse shear strain at the elastic axis
Γ_1	aerodynamic state in unstalled region in lift equation
Γ_2	aerodynamic state in stalled region in lift equation
Γ_{d_2}	aerodynamic state in stalled region in drag equation
Γ_{m_2}	aerodynamic state in stalled region in moment equation
λ	total inflow ratio
Λ_a	tip anhedral angle
Λ_s	tip sweep angle
η, ζ	blade cross-sectional principal axes coordinates
θ	pitch angle in degree
θ_0	mean value of pitch angle or main rotor collective pitch angle
θ_{0t}	tail rotor collective pitch angle
θ_{1c}, θ_{1s}	cyclic pitch angles for main rotor
Θ	fuselage attitude pitch
ρ	density of air
σ	main rotor solidity ratio
σ, σ_d, σ_m, $\overline{\sigma_m}$	parameters used in dynamic stall model
σ_{xx},$\sigma_{x\eta}$,$\sigma_{x\zeta}$	stress components
τ_0	initial twist rate of the blade
Ω_0	reference RPM of the rotor
ψ	azimuthal angle or nondimensional time, Ωt
ψ_k	azimuthal angle of the k^{th} blade
Ψ	cross-sectional warping function
ζ_k	local slope in lag bending of k^{th} blade
$(\ )_{,\eta}$	derivative of $(\ )$ $w.r.t.$ η
$(\ )_{,\eta\eta}$	double derivative of $(\ )$ $w.r.t.$ η
$(\ )'$	derivative $w.r.t.$ x
$\delta(\ )$	variation of $(\ )$
$(\ )_{,x}$	derivative of $(\ )$ $w.r.t.x$
$(\ )_{xx}$	double derivative of $(\ )$ $w.r.t.x$
$(\dot{\ })$	derivative $w.r.t.$ time

References

[1] D.L. Kunz. Comprehensive rotorcraft analysis : Past, present and future. In *46th AIAA Structural Dynamics & Materials Conference, AIAA 2005-2244*, Austin, Texas, 2005.

[2] K.C. Kim and I. Chopra. Aeroelastic analysis of swept, anhedral, and tapered tip rotor blades. *Journal of the American Helicopter Society*, 37(1), 1986.

[3] K.A. Yuan, P.P. Friedmann, and C. Venkatesan. A new aeroelastic model for composite rotor blades with straight and swept tips. In *33rd AIAA Structural Dynamics & Materials Conference, AIAA 92-2259*, Dallas, Texas, 1992.

[4] C.J. He. *Development and Application of a Generalized Dynamic Wake Theory for Lifting Rotors*. PhD thesis, Georgia Institute of Technology, Atlanta, July 1989.

[5] D. Petot. Differential equation modeling of dynamic stall. *La Reserche Aerospatiale*, (1989-5), 1989.

[6] A. Datta, M. Nixon, and I. Chopra. Review of rotor loads prediction with the emergence of rotorcraft cfd. *Journal of the American Helicopter Society*, 52(4), October 2007.

[7] B. Glaz, L. Liu, P.P. Friedmann, J. Bain, and L.N. Sankar. A surrogate-based approach to reduced-order dynamic stall modeling. *Journal of the American Helicopter Society*, 57(2), 2012.

[8] W. Johnson. A history of rotorcraft comprehensive analyses. Technical report, NASA/TP-2012-216012, April 2012.

[9] V. Laxman and C. Venkatesan. Influence of dynamic stall and dynamic wake effects on helicopter trim and rotor loads. *Journal of the American Helicopter Society*, 54(3), 2009.

[10] M. Rohin Kumar and C. Venkatesan. Aeroelastic analysis of a helicopter in steady maneuver using dynamic wake/dynamic stall models. In *European Rotorcraft Forum*, Moscow, Russia, September 2013.

[11] M. Rohin Kumar and C. Venkatesan. Effects of rotor blade tip geometry on helicopter trim and control response. In *AHS Aeromechanics Specialists Conference*, SanFrancisco, USA, January 2014.

[12] M. Rohin Kumar. *Comprehensive Aeroelastic and Flight Dynamic Formulation for the Prediction of Loads and Control Response of a Helicopter in General Maneuvering Flight*. PhD thesis, Indian Institute of Technology, Kanpur, February 2014.

[13] G. Wempner. *Mechanics of solids with applications to thin bodies*, volume 2. Springer, 1981.

[14] B. Panda. Technical note: Assembly of moderate-rotation finite elements used in helicopter rotor dynamics. *Journal of the American Helicopter Society*, 32(4), 1987.

[15] V. Laxman and C. Venkatesan. Chaotic response of an airfoil due to aeroelastic coupling and dynamic stall. *AIAA journal*, 45(1), 2007.

[16] G.D. Padfield. *Helicopter Flight Dynamics*. John Wiley & Sons, 2008.

[17] GSL - GNU scientific library. http://www.gnu.org/software/gsl/.

[18] J.J. Epps and R. Chandra. The natural frequencies of rotating composite beams with tip sweep. *Journal of the American Helicopter Society*, 41(1), 1996.

[19] A.S. Hopkins and R.A. Ormiston. An examination of selected problems in rotor blade structural mechanics and dynamics. *Journal of the American Helicopter Society*, 51(1), 2006.

[20] D.L. Sharpe. An experimental investigation of the flap-lag-torsion aeroelastic stability of a small-scale hingeless helicopter rotor in hover. Technical report, NASA TP 2546, January 1986.

[21] K. Götzfried. Survey of tiger main rotor loads from design to flight test. *Journal of the American Helicopter Society*, 47(4), October 2002.

[22] G.D. Singh. Helicopter flight dynamics simulation for analysis of trim, stability and control. Master's thesis, Indian Institute of Technology, Kanpur, May 2012.

Table 1: Rotor data

Parameter		Value
Number of blades,	N_b	4
Air density at sea level,	ρ (kg/m^3)	1.224
Blade mass distribution,	m_0 (kg/m)	8.45
Non-dimensional blade chord,	c/R	0.0757
Solidity ratio,	σ	0.09646
Weight coefficient,	C_w	0.00734
Pre-twist,	$\theta_{tw}(deg)$	-12
lift-curve slope,	$C_{l\alpha}$	5.73
Profile drag coefficient,	C_{d0}	0.01
Lock number,	γ	6.4
Torque offset,	a/R	0.0015
Predroop,	$\beta_d(deg)$	2.5
Blade Frequency data: Nondimensional		
Lag modes		0.713
		5.291
Flap modes		1.098
		2.881
		5.010
		7.582
Torsional mode		4.372
Axial mode		33.341

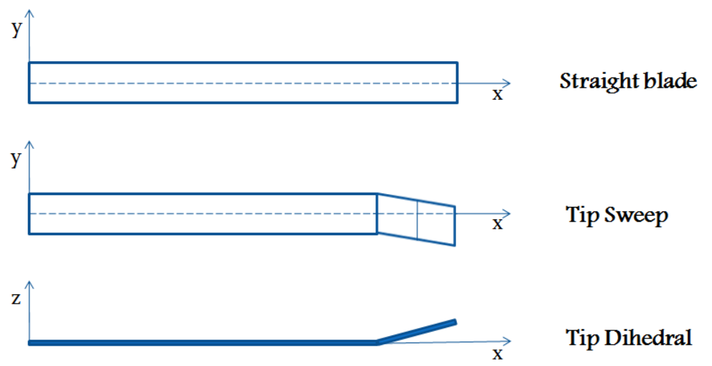

Figure 1: Sign convention for blade tip geometry

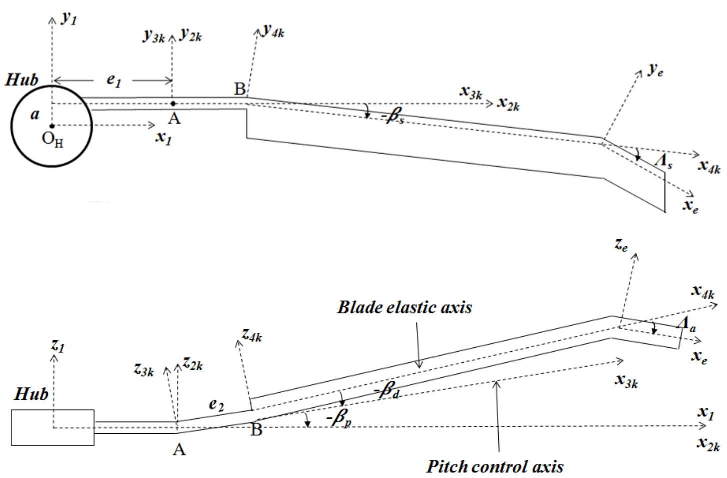

Figure 2: Blade coordinate systems (a) Blade top view (b) Blade front view

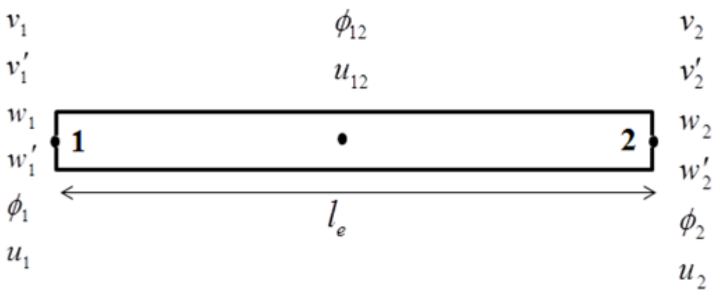

Figure 3: Element nodal degrees of freedom

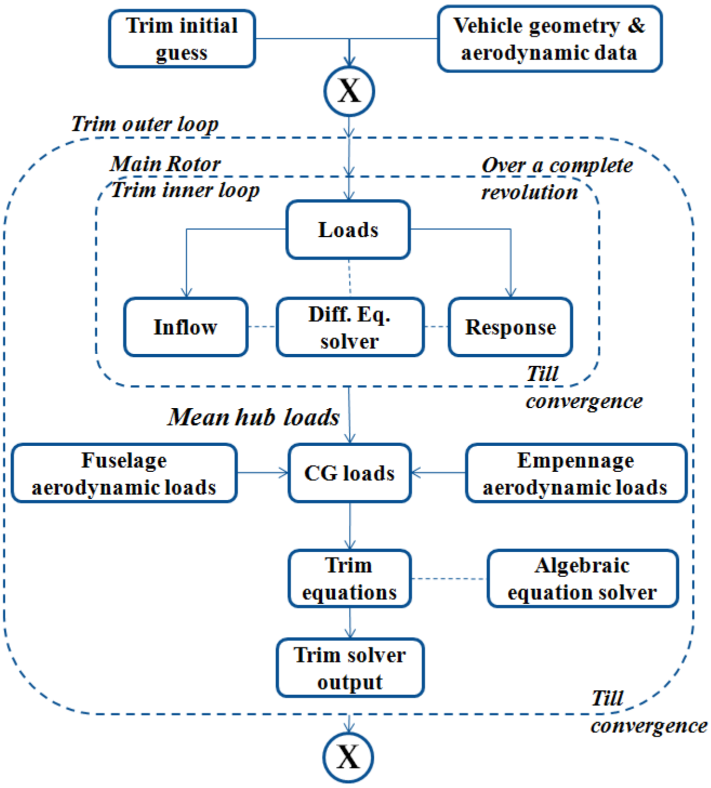

Figure 4: Flowchart for helicopter trim and rotor response

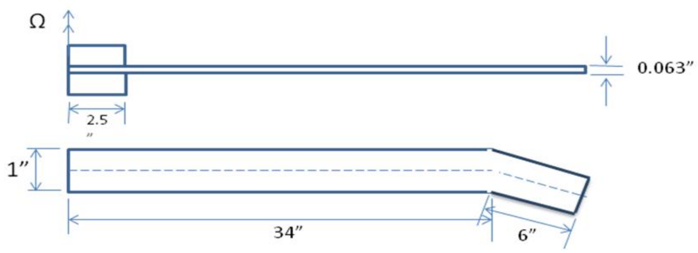

Figure 5: Geometric details of Vacuum Chamber Experiment beam

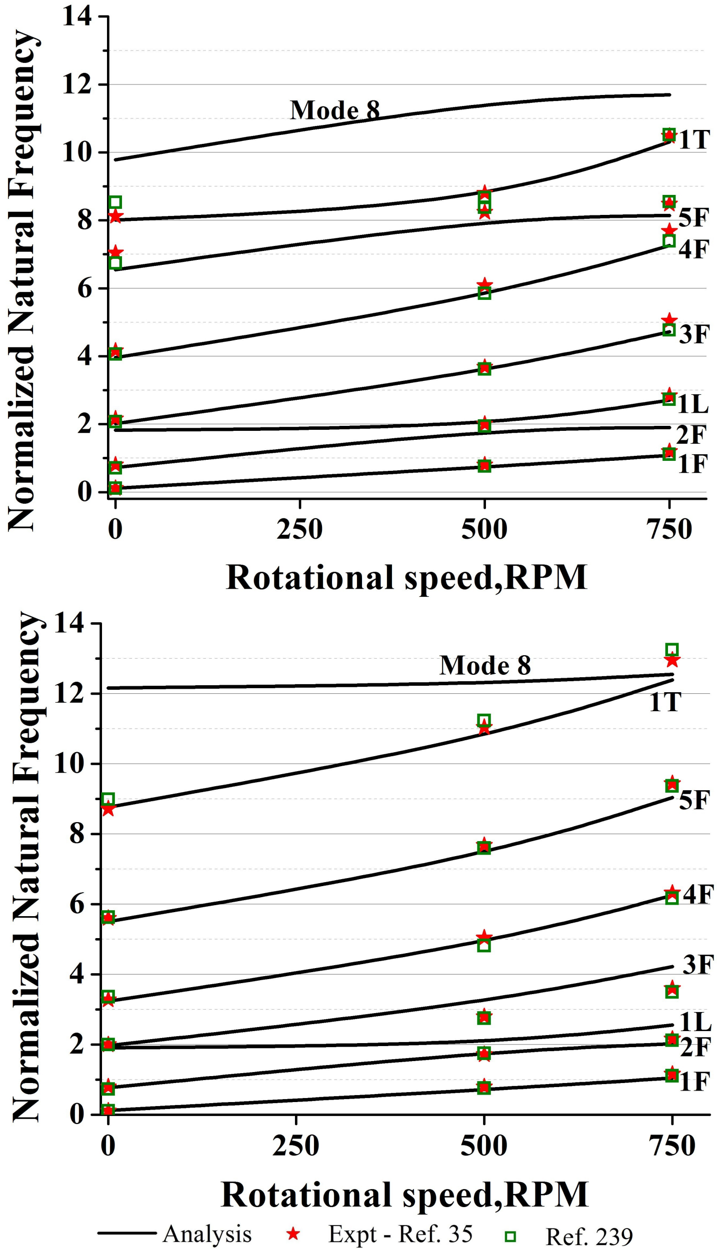

Figure 6: Effect of RPM on natural frequencies for (a) $\Lambda = 0^0$ and (b) $\Lambda = 45^0$

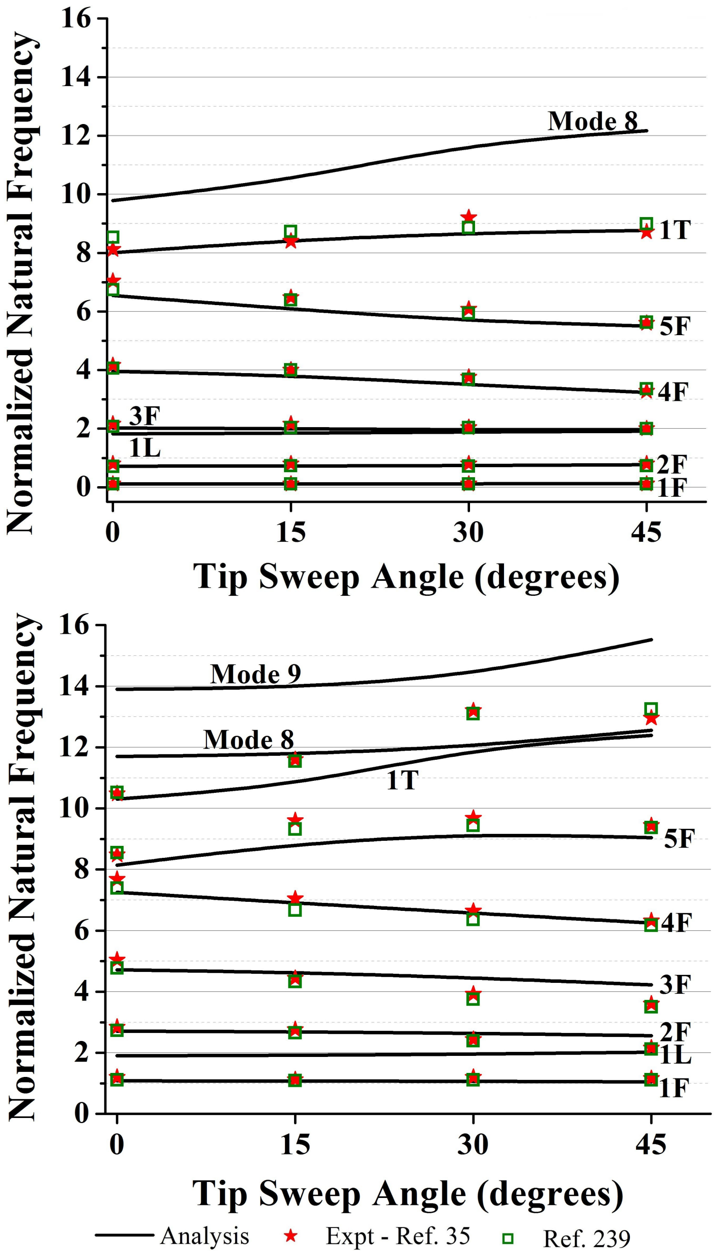

Figure 7: Effect of Sweep on natural frequencies for (a) $\Omega = 0$ RPM and (b) $\Omega = 750$ RPM

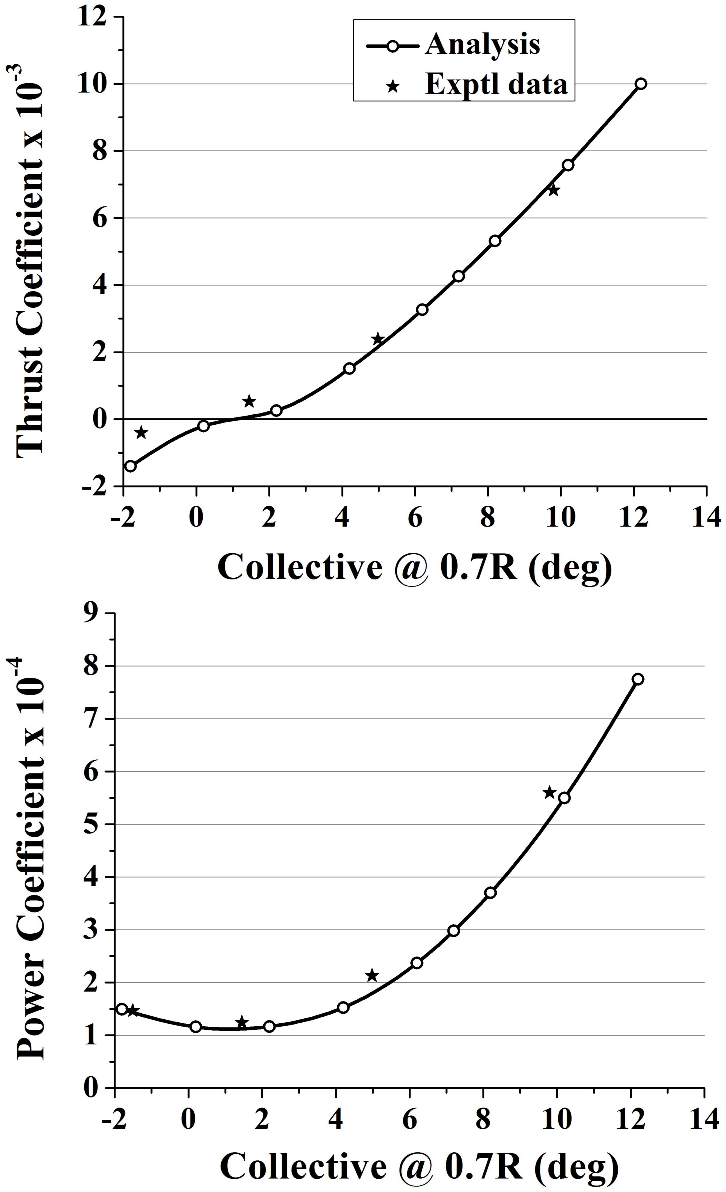

Figure 8: (a)Thrust (C_T) and (b)Power (C_P) curves

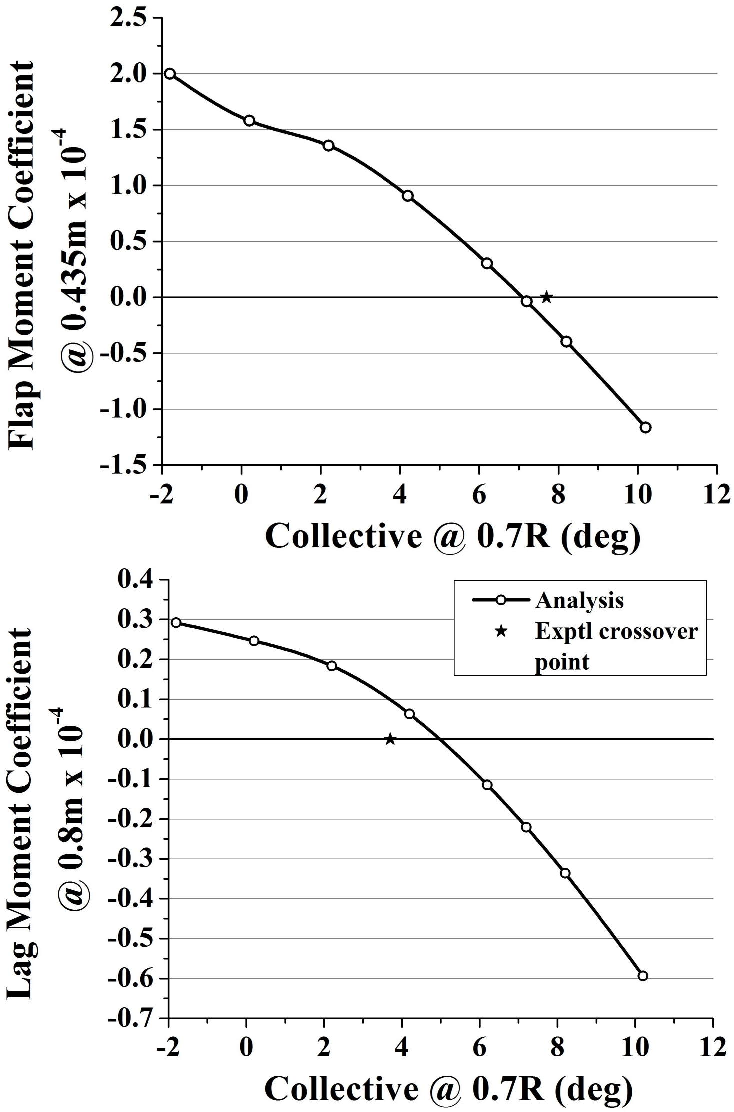

Figure 9: Bending moments variation with collective angles

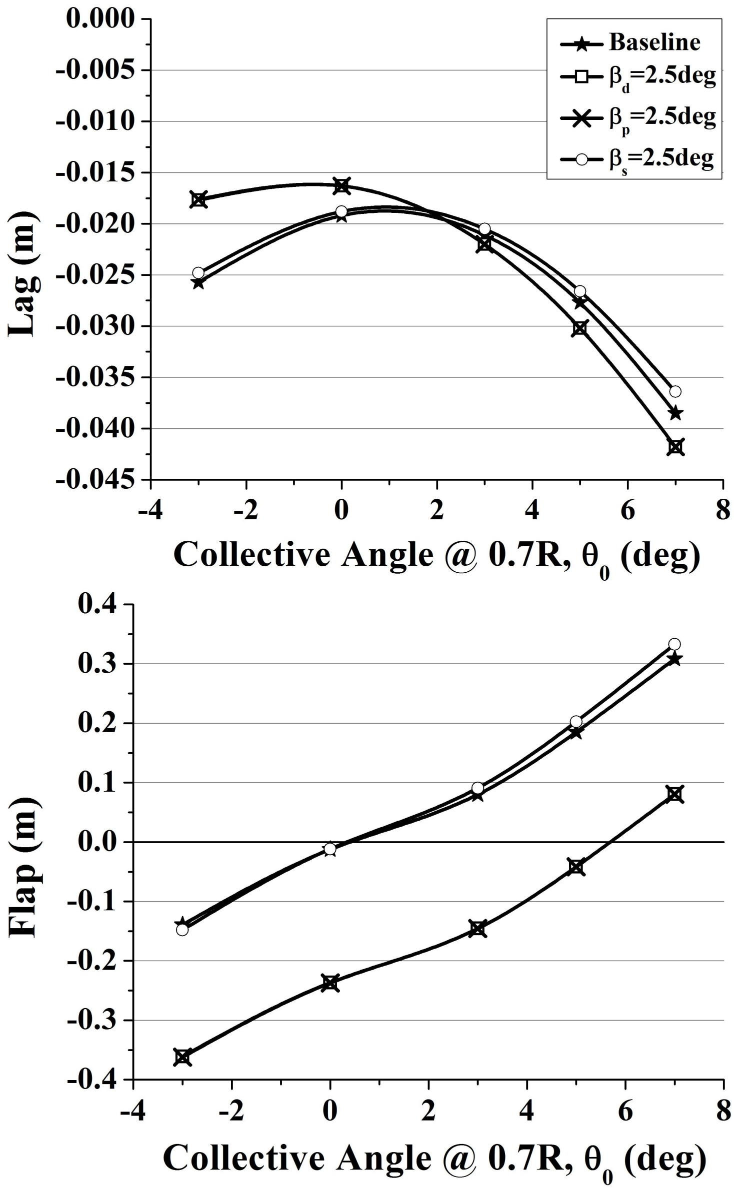

Figure 10: Effects of blade predroop (β_d), precone (β_p) and presweep (β_s) on lag and flap responses

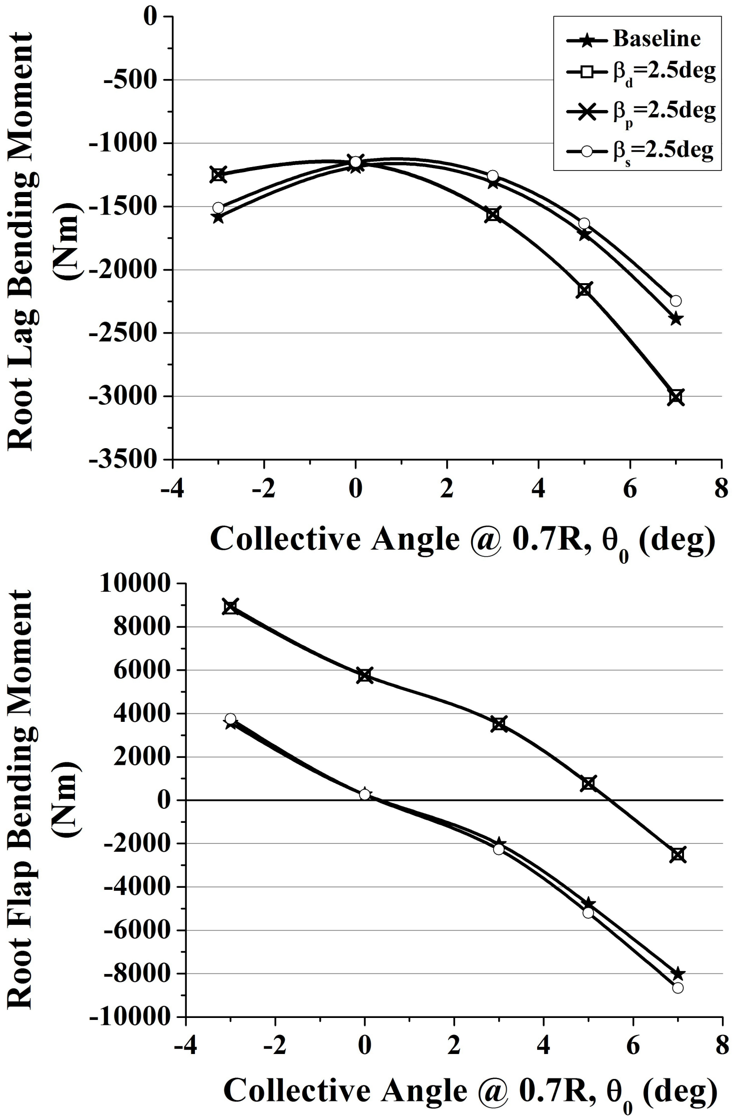

Figure 11: Effects of blade predroop (β_d), precone (β_p) and presweep (β_s) on root lag and flap bending moments

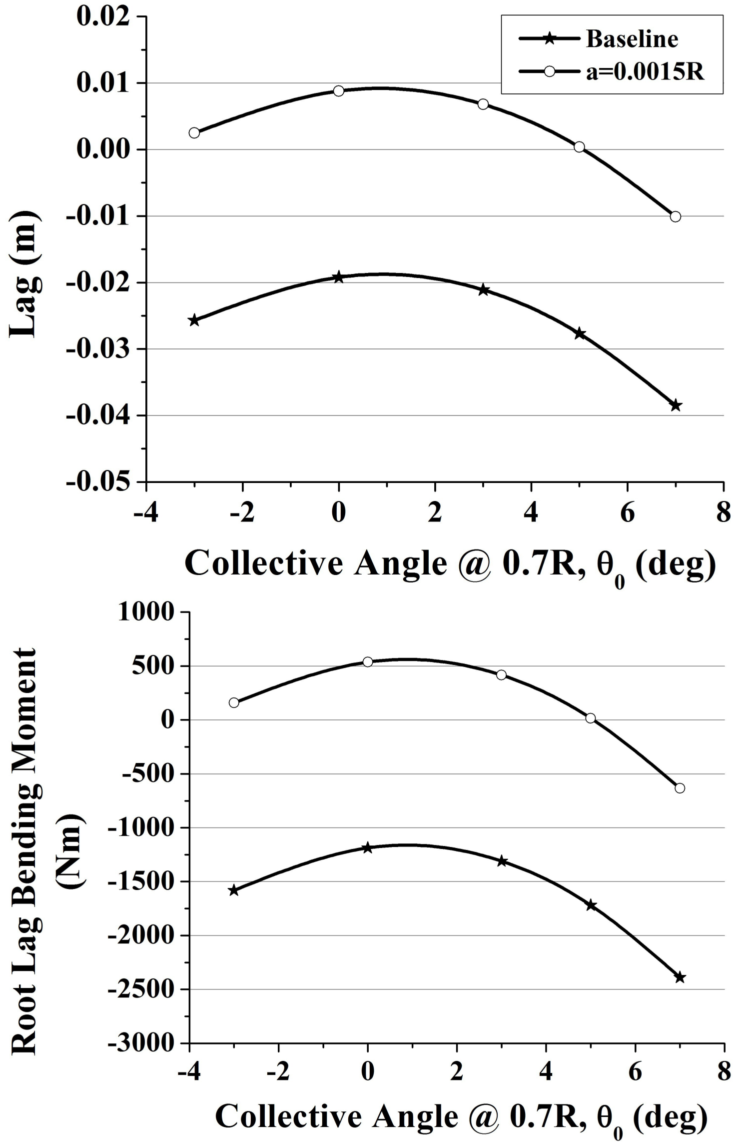

Figure 12: Effects of torque offset on blade lag response and root lag bending moment

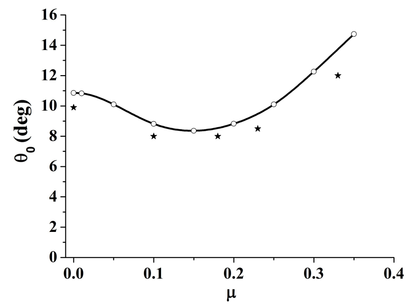

Main rotor collective

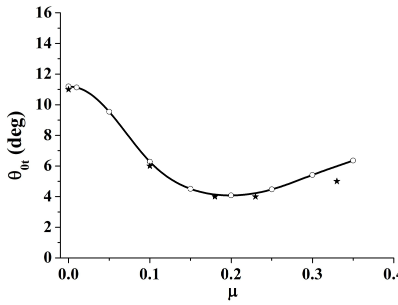

Tail rotor collective

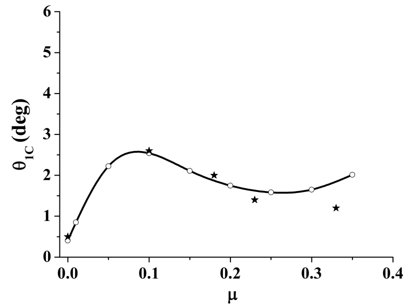

Lateral cyclic

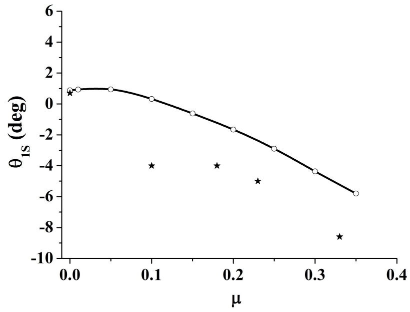

Longitudinal cyclic

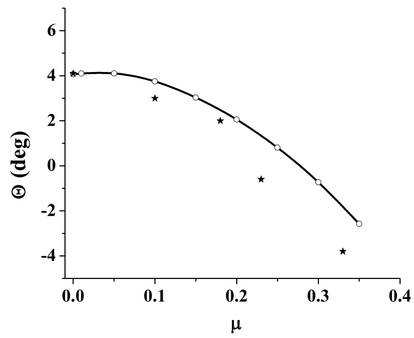

Pitch attitude

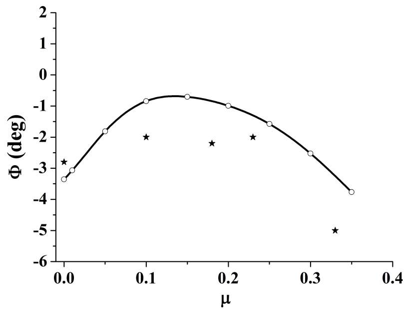

Roll attitude

Figure 13: Trim variation with forward speed